



LAWRENCE
LIVERMORE
NATIONAL
LABORATORY

A New Incorporation Mechanism for Trivalent Actinides into Bio-Apatite: A Time Resolved Laser Fluorescence and Extended X-ray Absorption Fine Structure Study

K. Holliday, S. Handley-Sidhu, K. Dardenne, J. Renshaw, L. Macaskie, C. Walther, T. Stumpf

January 3, 2012

A New Incorporation Mechanism for Trivalent Actinides into Bio-Apatite: a TRLFS and EXAFS Study

Disclaimer

This document was prepared as an account of work sponsored by an agency of the United States government. Neither the United States government nor Lawrence Livermore National Security, LLC, nor any of their employees makes any warranty, expressed or implied, or assumes any legal liability or responsibility for the accuracy, completeness, or usefulness of any information, apparatus, product, or process disclosed, or represents that its use would not infringe privately owned rights. Reference herein to any specific commercial product, process, or service by trade name, trademark, manufacturer, or otherwise does not necessarily constitute or imply its endorsement, recommendation, or favoring by the United States government or Lawrence Livermore National Security, LLC. The views and opinions of authors expressed herein do not necessarily state or reflect those of the United States government or Lawrence Livermore National Security, LLC, and shall not be used for advertising or product endorsement purposes.

1 A new incorporation mechanism for trivalent actinides into bio-apatite: a TRLFS and EXAFS study

2
3 Kiel Holliday^{1,2}, Stephanie Handley-Sidhu³, Kathy Dardenne¹, Joanna Renshaw³, Lynne Macaskie⁴,

4 Clemens Walther¹, Thorsten Stumpf¹

5 ¹Institute for Nuclear Waste Disposal, Karlsruhe Institute for Technology, 1 Hermann-von

6 Helmholtz-platz, Eggenstein-Leopoldshafen 76344 Germany

7 ²Lawrence Livermore National Lab, 7000 East Ave., Livermore, CA 94551 USA

8 ³School of Geography, Earth and Environmental Sciences, ⁴School of Biosciences, University of

9 Birmingham, Edgbaston, Birmingham, B15 2TT UK

10
11 **One of the most toxic byproducts of nuclear power and weapons production are the**
12 **transuranics, which have a high radiotoxicity and long biological half-life due to their**
13 **tendency to accumulate in the skeletal system. This accumulation is inhomogeneous and has**
14 **been associated with the chemical properties and structure of the bone material rather than**
15 **its location or function. This suggests a chemical driving force to incorporation and requires**
16 **an atomic scale mechanistic understanding of the incorporation process. Here we propose a**
17 **new incorporation mechanism for trivalent actinides and lanthanides into synthetic and**
18 **biologically produced hydroxyapatite. TRLFS and EXAFS have been used to prove that**
19 **trivalent actinides and lanthanides incorporate into the amorphous grain boundaries of**
20 **apatite. This incorporation site can be used to explain patterns in uptake and distribution of**
21 **radionuclides in the mammalian skeletal system.**

22 23 INTRODUCTION

24 One of the most toxic byproducts of nuclear power and weapons production are the transuranics
25 due to their long biological half-life and high radiotoxicity. For instance, Pu, Am and Cm have been
26 identified as more carcinogenic than Ra at similar activities due to the inhomogeneous nature of

their distribution in the skeletal system^{1,2,3}. As much as 70% of these radionuclides are deposited into the bone material leading to long biological half lives^{4,5}. This inhomogeneous distribution has been shown to be dependent on the chemical properties and structure of the bone and not its location or function^{2,4}. This would suggest that incorporation and retention of radionuclides within biological hard tissue, consisting mostly of hydroxyapatite, is dependent on the chemical incorporation mechanism independent of biological function. The chemical form and solubility of the transuranics such as Pu, Am and Cm has been shown to have considerable influence on uptake in the skeletal system^{6,7}. This has lead to the investigation of different treatments, such as DTPA, to limit the retention of these radionuclides⁸. These treatments while limiting uptake in the liver have little effect on the uptake by the skeletal system, despite evidence that long term deposition into hard tissue can take days^{8,9}.

There is, therefore, a need to develop an atomic scale mechanistic understanding of the incorporation process at the solid-solution interface so that treatment can better address the process of actinide deposition in biological hard tissue. By using apatite, the main component of bone material, one can study a well defined single component approximating the behavior of biological hard tissue. Previous work has been performed with lanthanide homologs of the trivalent actinides on post-incorporation heat treated samples of apatite by X-ray diffraction (XRD)¹⁰⁻¹³, extended X-ray absorption fine structure (EXAFS)¹⁴, and time resolved laser fluorescence spectroscopy (TRLFS)¹⁵⁻¹⁷. These studies on heated samples are irrelevant to the incorporation at room temperature since it has been shown that the speciation is different before heat treatment^{18,19}. Two key studies have focused on the speciation of Eu^{3+} (an analogue for trivalent actinide ions) in apatite at room temperature by TRLFS. Both studies concluded that Eu^{3+} was incorporated into the C_3 symmetry Ca(I) site of apatite^{18,19}. In the first study, all reported emission spectra had more peaks than would be permitted by C_3 symmetry which was explained as emission lines arising from impurities in the naturally occurring apatite samples used for the study¹⁸. The second study eliminated this possibility by using synthetic apatite and produced similar emission spectra¹⁹. It was

also concluded to be Eu^{3+} substituting on the Ca(I) site because of being trapped by the co-precipitation process. Although site selective excitation was used in this later study, the emission spectra had a poor resolution at room temperature, and it is not possible to clearly resolve the splitting to make a definitive statement on the symmetry of the Eu^{3+} . Only one study was performed under similar conditions with actinides, namely Cm, where it was concluded that Cm^{3+} incorporates into the apatite structure unlike other phosphate mineral phases such as $\text{Th}_4\text{P}_6\text{O}_{23}$, ZrP_2O_7 and $\text{Zr}_2\text{O}(\text{PO}_4)_2$ in which only surface sorption was evident²⁰. No speculation was made on the site of incorporation in the Cm study.

METHODS

Hydroxyapatite synthesis. Hydroxyapatite was synthesized by coprecipitation of calcium and phosphate at basic pH. All chemicals were reagent grade and purchased from Alpha Aesar. Concentrated solutions of calcium chloride and sodium hydrogen phosphate were made by dissolving in 18 M Ω water. These solutions were then mixed in a 5:3 calcium to phosphate ratio and brought to pH 11 with sodium hydroxide. The solution was stirred for 24 hours before the solid was collected via filtration. This solid was dried and subsequently heated to 700 °C to improve crystallinity.

Bio-apatite synthesis. *Serratia* sp. NCIMB 40259 was used with kind permission of Isis Innovation, Oxford, UK³². Biofilm-loaded foam cubes (prewashed in isotonic saline; ~4.5 mg dry cell mass/cube) were placed in flasks containing 50 mL TAPSO/NaOH buffer (50 mM; pH 9.2) with 5 mM glycerol 2-phosphate (G2P) and 1 mM CaCl_2 . The volume lost to evaporation was replaced daily with the same solutions over the 8 day synthesis, after which the material was dislodged by a gentle tapping and squeezing action. The remaining solid was washed with acetone, air dried, and characterized by scanning electron microscope and X-ray diffraction³³.

X-ray diffraction (XRD). Samples were ground to a fine powder and spread in a thin layer over a low-background sample holder (single crystal silicon wafer) with the aid of methanol. The powder XRD patterns were collected on a Bruker D8 Advance diffractometer, using a Cu anode

(wavelength $K\alpha_1$ at 0.1540598 nm). Patterns were taken using an acceleration of 40 mV and current of 40 mA over a range from 10 to 120 °2 θ with a step size of 0.01 °2 θ and 4 seconds per step.

Phases were identified using Bruker-AXS EVA software.

Batch studies. Batch studies were performed simply by placing the solution containing the doping ion in contact with hydroxyapatite, while controlling ionic strength, solid to liquid ratio, pH, and doping ion concentration. The solution containing the doping ion was 2.0 mM sodium perchlorate to maintain ionic strength and was adjusted to pH of 6 with sodium hydroxide and perchloric acid as needed before being added to hydroxyapatite at a solid to liquid ratio of 2.0 g/L. The Cm concentration was 0.08 μ M (taken from stock solution) and the Eu concentration was 1.0 μ M. Samples were occasionally stirred over the contact time of 21 days. The isotopic composition of the long-lived curium solution (20.0 μ M) is 97.3 % Cm–248, 2.6% Cm–246, 0.04% Cm–245, 0.02% Cm–247 and 0.009% Cm–244 in 1.0 M HClO₄.

Time resolved laser fluorescence spectroscopy (TRLFS). TRLFS was performed using a pulsed (20 Hz) XeCl-eximer laser (Lambda Physics, EMG, 308 nm) pumped dye laser (Lambda Scanmate). The following dyes were used: QUI for UV excitation, Rhodamine 6G for direct excitation of Eu, and Rhodamine B for direct excitation of Cm. Indirect excitation of Eu and Cm was performed at 394.0 nm and 396.6 nm respectively. The range used for the direct excitation of Eu was 575 – 582 nm, and the direct excitation of Cm was performed at 600 – 612 nm. The laser wavelength was monitored using a Toptica WS7 wavemeter ($>10^{-5}$ nm accuracy). Fluorescence measurements were detected by an optical multichannel analyzer that consists of a polychromator with 300/600/1200 lines/mm gratings (Jobin Yvon) and an intensified, gated photodiode array (Spectroscopy Instruments). Maximum resolution at 300 and 1200 lines/mm was measured to be 0.9 and 0.2 nm, respectively. The detection system was calibrated with a neon lamp (Pen Ray 6032). The samples were cooled to < 20 K by a helium refrigerated cryostat (CTI-cryogenics) to improve resolution. For the discrimination of Rayleigh and Raman scattering the minimum gate delay between laser pulse and camera gating was set to 1.0 μ s. The gate width of the camera was

fixed at 10 ms to ensure the collection of the entire fluorescence signal. Fluorescence lifetime measurements were made with a delay time step between 15 and 200 μ s and a total of 60 steps were taken for each lifetime measurement.

Extended x-ray absorption fine structure (EXAFS). Europium L3-edge and L2-edge spectra were recorded at the INE beamline at ANKA (Germany) using a double-crystal monochromator (DCM) equipped with a pair of Si(111) crystals. The DCM is operated in fixed-exit mode. The incident intensity is held constant by means of a piezo-driven feedback system. The parallel alignment of the crystal faces is detuned to $\sim 70\%$ of the maximum beam intensity. The samples powders were mounted in Kapton[®] tape. Measurements were made in fluorescence mode using a five element Ge detector with a sample orientation of 45° to the incident beam. The energy calibration was performed using a Fe metal foil (K edge at 7112 eV). EXAFS data analysis was performed using standard procedures in Athena and Artemis³⁴ interfaces of the iFEFFIT software³⁵. The phase and amplitude data used for data analysis are calculated for a 15 atom cluster derived from the undoped apatite structure. Single path scattering files for phase and amplitude are used too for comparison. The k-range used for the fit is 2.669-8.715 \AA^{-1} and fits are performed in the R-space on the k^2 -weighted data. The overall scaling factor S_0^2 was held constant at 0.85 after its determination on a standard sample. Distances are determined with an error of 0.02 \AA and coordination numbers with an error of 20%.

RESULTS AND DISCUSSION

TRLFS of Eu^{3+} doped hydroxyapatite

This study uses site selective TRLFS of Eu doped at 100 ppm in synthetic hydroxyapatite to eliminate extraneous peaks from multiple sites or impurities. Measurements were performed at deep temperatures (< 20 K) for improved resolution. Despite correcting previous explanations of impurities and multiple site excitation, the same emission spectra found in literature are produced^{18,19} with a clear 3-fold splitting observed for the $^5\text{D}_0 \rightarrow ^7\text{F}_1$ transition, indicating less than

C₃ symmetry (Fig. 1a). This eliminates the Ca(I) site of apatite as the location of the incorporating Eu³⁺ ion.

It should be noted that this cannot be a substitution in the lower symmetry Ca(II) site since the Eu³⁺ can be driven there by heating, producing a different emission spectrum well documented to be Eu³⁺ substituted in the Ca(II) site with C₁ symmetry¹⁵⁻¹⁷ (supplemental Figure 1). It is also unlikely that this large and reproducible of a disturbance in the local symmetry is due to charge compensation. Previous studies of Eu³⁺ and Cm³⁺ substitution onto calcium sites in other structures have produced clear evidence of the original symmetry of the site occupied, despite slight disturbances attributed to charge compensation²¹⁻²³. A surface species can also be eliminated as the explanation for increased splitting of the F₁ transition because of the presence of a long, although bi-exponential, fluorescence lifetime (Fig. 1b). The fluorescence lifetime has a short component of 0.6 ms, which can be attributed to a single water or two hydroxide molecules in the immediate coordination sphere with the equation derived by Horrocks and Sudnick²⁴. The long component (2.0 ms) is an indication of the absence of water and hydroxide in the immediate coordination sphere, clearly indicating incorporation rather than surface sorption. An excitation spectrum was obtained by integrating the total fluorescence over the ⁵D₀ → ⁷F_{0,1,2} transitions while varying the excitation wavelength in the range of the ⁵D₀ → ⁷F₀ transition. In this region a single peak results from each unique Eu³⁺ environment due to the singular degeneracy of ΔJ = 0. This produced an extremely broad peak from 577 nm to 580 nm indicating a poorly defined local environment around the incorporated Eu³⁺ (Fig. 1c). The kinetics of incorporation is fast as there appears to be no significant change in spectra or fluorescence lifetime after one hour (Figure 1).

The fluorescence lifetime proves an incorporated species (Fig. 1b) and emission spectra indicate that Eu³⁺ does not substitute for either Ca site within the apatite crystal structure (Fig. 1a). This along with evidence of a poorly defined Eu³⁺ environment from the excitation spectrum (Fig. 1c) leads to the conclusion that Eu³⁺ is incorporating into the amorphous grain boundaries of the polycrystalline apatite. This explanation was further supported when the study was expanded to

biologically produced apatite, which should better represent the low crystallinity of biological hard tissue.

It has recently been shown that biologically produced apatite has a greater affinity and capacity to incorporate various cations²⁵. A characterization of the material led to two possible explanations²⁶. The first was that the biological residue could not be completely eliminated from the sample. This biological residue could participate in the incorporation process or add additional sites that could accommodate the Eu^{3+} ion. The second explanation was a difference in microstructure. Although both biologically produced and synthetic apatites are similar polycrystalline powders, they have been shown to have a drastic difference in crystalline grain size. Here crystalline grain size being the size of a crystalline domain with a singular orientation within a polycrystalline particle. The bioapatite was measured to have crystalline grains of 25 nm while the synthetic apatite has crystalline grains at the μm scale. This large difference in crystalline grain size leads to a much higher proportion of amorphous grain boundary in the biologically produced apatite that could result in a greater uptake of trivalent cations. This biological apatite better approximates biological hard tissue, which has a greater amorphous component.

TRLFS was performed in an effort to determine if there was a change in speciation or an additional incorporation site due to the biological material residue. The excitation spectrum shows a broad peak that compares well to that obtained for synthetic apatites, indicating a poorly defined environment around the Eu^{3+} , as would be expected of an amorphous environment (Fig 2a). The fluorescence lifetime was also similar for both biologically produced and synthetic apatite (Fig 2b). The most compelling evidence was the fact that the fluorescence emission spectra are identical (Fig 2c). This is definitive proof of the same speciation in both samples, which eliminates biological residue as a possible explanation for the increase in uptake in the case of trivalent actinides and lanthanides. The most probable explanation is, therefore, the increased amorphous grain boundary proportion in biologically produced apatite results in an increase uptake of cations.

Structural determination with EXAFS

Extended X-ray absorption fine structure (EXAFS) was performed as a complimentary probe of the local environment and structure of the incorporated Eu^{3+} . The results for synthetic and biologically produced apatite were similar with the exception that trace amounts of Fe present in biologically produced apatite only allowed for measurements up to $k = 6.1 \text{ \AA}^{-1}$ (Supplemental Table 1). Because of this, only results for synthetic hydroxyapatite are presented and compared to expected values for that of the Ca(I) site in hydroxyapatite (ICSD #22059) in Table 1.

The distance from the incorporated Eu^{3+} to nearest neighbor oxygens was fit with a single shell, because a two shell approach did not significantly improve the fit or lower the Debye-Waller factor (Fig. 3). For comparison, distances in the referenced Ca(I) site of hydroxyapatite are given as a weighted average, although it is recognized that the nearest neighbor oxygen atoms occur at two distinct distances. The first shell oxygen atoms were pulled closer to the Eu^{3+} atom than the Ca(I) site crystal structure by 0.16 \AA . It could be argued that this was a distortion due to the incorporation of Eu^{3+} as a solid solution although the effect is larger than expected for the difference in radii (0.04 \AA) when compared to other solid solutions²⁷. This effect is consistent with an amorphous material which would have more flexibility in bond distances. The coordination number has also dropped from 9 in the solid solution to 7.9. This was also measured in EXAFS studies of Eu phosphate glass²⁸, although it should be noted that this is not significantly different given the large uncertainty in coordination number in EXAFS measurements. Nevertheless, a drop of the coordination number is fully consistent with a diminution of the bond length. The next shell was fit with phosphate and shows no significant difference from the hydroxyapatite, although none could be expected given previous studies of amorphous phosphates²⁸.

Definitive proof that Eu^{3+} was not incorporated into the Ca(I) site of apatite was shown in the Eu – Ca shell as compared to the Ca(I) – Ca distance. Here any effect due to the isomorphic substitution of Eu^{3+} for Ca would have dissipated. The Eu^{3+} data shows an increase in coordination number when compared to the Ca(I) site; however, the most striking difference was an increase in

the Eu – Ca interaction distance by 0.65 Å longer than the Ca(I) – Ca distance. It should be noted that these results are also inconsistent with substitution on the Ca(II) site as was already established for samples after heat treatment¹⁸. This can only be explained by a complete break with the crystal structure of hydroxyapatite and eliminates the possibility of Eu³⁺ incorporating through isomorphic substitution within apatite at room temperature. The EXAFS data thereby confirmed what was suggested by TRLFS. Eu³⁺ is incorporating into the amorphous grain boundaries of synthetic and biologically produced hydroxyapatite.

Actinide containing material: Cm³⁺ studies

TRLFS was performed on Cm³⁺ containing hydroxyapatite and biologically produced hydroxyapatite in the same way that it was done for Eu³⁺ apatites. The emission spectra after UV excitation shows an extremely broad (FWHM = 10 nm) peak centered at 607 nm for synthetic and bioapatite, establishing the same local environment for trivalent actinides in both forms of apatite (Fig. 4a). The large peak width suggests a range of local environments which would also be expected for Cm³⁺ incorporated into the amorphous grain boundaries as was established for Eu³⁺ by TRLFS and EXAFS. The maximum emission wavelength was slightly higher in energy than the 609 nm that was previously reported²⁰. This is likely due to the published spectrum being collected at a longer delay time, which has the effect of shifting the peak to lower energy. This effect occurs because the range of species present exhibit shorter lifetimes at higher energies. The peak reported here at 607 nm still shows a stronger bathochromic shift than other examples of crystalline Cm³⁺ doped phosphates, such as the 8-fold coordinated LuPO₄²⁹ and 9-fold coordinated LaPO₄³⁰.

The excitation spectrum produced the same extremely broad peak as UV excitation with a large shoulder at higher energies (Fig. 4b). This shoulder was shown to be due to “hot band” excitation of the higher excited states and the large increase in intensity reinforces the assumption that a large range of Cm³⁺ environments exist. The fluorescence lifetimes in both samples were similar and fit to a bi-exponential lifetime (Fig. 4c). The short lived component of 235 μs can be attributed to two waters by the Kimura equation³¹. The longer lived lifetime of 850 μs shows a complete loss of the

hydration sphere indicating incorporation into the bulk. These results compare well to that obtained with Eu^{3+} .

Lastly, direct excitation was used to probe the region of Cm^{3+} fluorescence. It was proven through fluorescence line narrowing that the broad emission spectrum shown by UV excitation is in no way limited to the resolution of the instrument (Fig. 5). This demonstrated that the broad peak emission spectrum was due to a continuum of closely related sites. Such spectra would be expected from a sample with a poorly defined Cm^{3+} environment that has no long range order. This is presented as further proof that trivalent actinide and lanthanide incorporate into the amorphous grain boundaries of hydroxyapatite.

CONCLUSIONS AND IMPLICATIONS

We propose a new mechanism for trivalent actinide and lanthanide uptake into apatites: incorporation into the amorphous grain boundaries of the polycrystalline apatite and not incorporation onto a calcium site within the crystal structure as previously proposed. This has been proven in the current study by TRLFS and EXAFS of synthetic and biologically produced hydroxyapatite doped with Eu^{3+} and Cm^{3+} . This is in direct conflict with previous assumptions that incorporation took place as an isomorphic substitution on the Ca(I) site creating a solid solution. This new conclusion not only explains the current data presented in this manuscript, but also previously unexplained phenomena presented in the TRLFS of other Eu:apatite studies performed by incorporating ions at room temperature^{18,19}.

This proposed mechanism for the incorporation of trivalent actinides helps to understand the incorporation process and distribution of transuranics throughout the skeletal system of organisms exposed to transuranic elements. It has been shown that Pu, Am, and Cm have an inhomogeneous distribution in biological hard tissue leading to high local concentrations and consequently a higher radiotoxicity¹⁻⁴. This finding can now be revisited with the insight that these areas of high local concentration are most likely areas of low crystallinity. In areas of high crystallinity it would be assumed that surface sorption would be the main mode of retention. Because of the slow growth of

bones, it has been shown that incorporation can take days in areas where surface sorption is dominant⁹. This new insight would allow one to distinguish situations where a treatment to desorb radionuclides might be successful, from those where incorporation has most likely already taken place. Understanding the processes that govern the sorption and incorporation of radionuclides in biological hard tissue is envisioned as the first step in designing treatment to decrease the amount of radionuclides retained over long time periods by organisms exposed to trivalent actinides.

References

1. Priest, N. D. & Jackson S. *Int. J. Radiat. Biol.* **1977**, 32, 325-350.
2. Polig, E., Bruenger, F. W., Lloyd, R. D. & Miller, S. C. *Health Phys.* **1998**, 75, 251-258.
3. Wood, M. D., Beresford, N. A., Semenov, D. V., Yankovich, T. L. & Copplestone, D. *Radiat. Environ. Biophys.* **2010**, 49, 509-530.
4. McInroy, J. F., Boyd, H. A., Eutsler, B. C. & Romero, D. *Health Phys.* **1985**, 49, 587-621.
5. Thomas, R. G., Healy, J. W. & McInroy, J. F. *Health Physics* **1984**, 46, 839-844.
6. Fouillit, M., *et al.* *Int. J. Radiat. Biol.* **2004**, 80, 683-689.
7. Guilmette, R. A., Kanapilly, G. M., Lundgren, D. L. & Eidson, A. F. *Health Phys.* **1984**, 46, 845-858.
8. Guilmette, R. A. & Muggenburg, B. A. *Int. J. Radiat. Biol.* **1993**, 63, 395-403.
9. Talbot, R. J., Newton, D. & Warner, A. J. *Health Phys.* **1993**, 65, 41-46.
10. Fleet, M. E. & Pan, Y. *J. Solid State Chem.* **1994**, 112, 78-81.
11. Fleet, M. E. & Pan, Y. *Amer. Mineral.* **1995**, 80, 329-335.
12. Fleet, M. E. & Pan, Y. *Geochim. Cosmochim. Acta* **1997**, 61, 4745-4760.
13. Fleet, M. E., Liu, X. & Pan, Y. *Amer. Mineral.* **2000**, 85, 1437-1446.
14. Martin, P., Carlot, G., Chevarier, A., Den-Auwer, C. & Panczer, G. *J. Nucl. Mater.* **1999**, 275, 268-276.
15. Ryan, F. M., Warren, R. W., Hopkins, R. H. & Murphy, J. J. *Electrochem. Soc.* **1978**, 125, 1493-1498.

285 16 Ternane, R., Trabelsi-Ayedi, M., Kbir-Ariguib, N. & Piriou, B. *J. Lumin.* **1999**, *81*, 165-170.

286 17 Graeve, O. A., Kanakala, R., Madadi, A., Williams, B. C. & Glass, K. C. *Biomaterials* **2010**,
287 *31*, 4259-4267.

288 18 Gaft, M., *et al.* *J. Lumin.* **1997**, *72-74*, 572-574.

289 19 Karbowiak, M. & Hubert, S. *J. Alloy Compd.* **2000**, *302*, 87-93.

290 20 Cavellec, R., Lucas, C., Simoni, E., Hubert, S. & Edelstein, N. *Radiochim. Acta* **1998**, *82*, 221-
291 225.

292 21 Schmidt, M., Stumpf, T., Fernandes, M. M., Walther, C. & Fanghänel, T. *Angew. Chem. Int.*
293 *Ed.* **2008**, *47*, 5846-5850.

294 22 Fernandes, M. M., *et al.* *J. Colloid Interface Sci.* **2008**, *321*, 323-331.

295 23 Stumpf, T. & Fanghänel, T. *J. Colloid Interface Sci.* **2002**, *249*, 119-122.

296 24 Horrocks, W. D. W. & Sudnick, D.R. *J. Am. Chem. Soc.* **1979**, *101*, 334-340.

297 25 Handley-Sidhu, S., Renshaw, J. C., Yong, P., Kerley, R. & Macaskie, L. E. *Biotechnol. Lett.*
298 **2011**, *33*, 79-87.

299 26 Handley-Sidhu, S., *et al.* *Environ. Sci. Technol.* **2011**, *45*, 6986-6990.

300 27 Holliday, K., Hartmann, T., Poineau, F., Kennedy, J. R. & Czerwinski, K. *J. Nucl. Mater.* **2009**,
301 *393*, 224-229.

302 28 Mountjoy, G., *et al.* *J. Non-Cryst. Solids* **2001**, *279*, 20-27.

303 29 Murdoch, K.M., Edelstein, N.M., Boatner, L.A. & Abraham, M.M. *J. Chem. Phys.* **1996**, *105*,
304 2539-2547.

305 30 Holliday, K. S., *et al.* *Radiochim. Acta* DOI: 10.1524/ract.2012.1900.

306 31 Kimura, T. & Choppin, G.R. *J. Alloys Compd.* **1994**, *213/214*, 313-317.

307 32 Finlay, J. A., *et al.* *Biotechnol. Bioeng.* **1999**, *63*, 87-97.

308 33 Yong, P., Macaskie, L. E., Sammons, R. L. & Marquis, P. M. *Biotechnol. Lett.* **2004**, *26*, 1723-
309 1730.

310 34 Ravel, B., Newville, M. *J. Synchrotron Rad.* **2005**, *12*, 537.

311 35 Newville, M. J. *Synchrotron Rad.* **2001**, 8, 322.

312
313 **Acknowledgements** We would like to thank Sebastian Büchner for technical assistance with
314 TRLS measurements and Claire Mennan for assistance with preparation of *Serratia sp.* This work
315 was cofinanced by the Helmholtz Gemeinschaft Deutscher Forschungszentren (HGF) by supporting
316 the Helmholtz-Hochschul-Nachwuchsgruppe “Aufklärung geochemischer Reaktionsmechanismen
317 an der Wasser/Mineralphasen Grenzfläche” and the EPSRC (EP/G063699/1). We thank the ANKA
318 synchrotron source for providing the beamtime. This work was performed under the auspices of the
319 U.S. Department of Energy by Lawrence Livermore National Laboratory under Contract DE-AC52-
320 07NA27344 and by the Department of Homeland Security, Domestic Nuclear Detection Office
321 under Contract HSHQDC-07-C-00034.

322 **Additional Information** The authors declare no competing financial interests. Supplementary
323 information is linked to the online version of the paper at <http://pubs.acs.org/Langmuir>

324 Correspondence and requests for materials should be addressed to K.H. (holliday7@llnl.gov) or
325 T.S. (thorsten.stumpf@kit.edu).

Table 1 EXAFS fitted parameters compared to that of the Ca(I) site. Typical error associated with coordination number is 20 % while reported bond distances are ± 0.02 Å. The k-range of fitting was 2.669-8.715 Å⁻¹. The R-range of fitting was 1.341-4.262 Å. The goodness of fit can be expressed as the difference of the fit and experimental data as a percent referred to as the residual, which was 1.2 % for hydroxyapatite.

Bond	R (Å)	N	σ^2 (Å ²)	E ₀ (eV)
Eu - O	2.39	7.9	0.004	4.6
Ca(I) - O	2.55	9.0	-	-
Eu - P	3.21	4.2	0.0002	10.7
Ca(I) - P	3.21	3.0	-	-
Eu - Ca	4.11	3.7	0.0004	11.8
Ca(I) - Ca	3.44	2.0	-	-

Figure Captions

Figure 1 TRLFS of Eu³⁺ in synthetic hydroxyapatite which shows little change over the contact time of 522 h. a) Emission spectra with 3-fold splitting of the F₁ transition indicating a lower local symmetry than the C₃ expected for the Ca(I) site of hydroxyapatite. b) Fluorescence lifetime measurements showing incorporation of the Eu³⁺ although multiple species exist. c) Excitation spectra with extremely broad peak suggesting poorly defined Eu³⁺ environment as would be expected in an amorphous environment.

Figure 2 TRLFS of Eu³⁺ in biologically produced apatite as compared to synthetic apatite. a) Excitation spectra with broad peak comparable to previous analysis of synthetic apatite suggesting amorphous environment. b) Lifetime measurements comparable to synthetic apatite confirming incorporation. c) Emission spectra from bio-apatite as compared to the synthetic hydroxyapatite indicating the same incorporated Eu³⁺ environment suggesting the same incorporation mechanism and excluding biological residue as an incorporation site.

Figure 3 EXAFS data with fit of synthetic hydroxyapatite a) FT magnitude (thick solid line), imaginary part (thin solid line), and fit results (open triangles and circles). FT is performed in the

range 1.341-4.262 Å. b) k^2 -weighted Eu L3 EXAFS of the sample (solid line) and fit result (open circles). Data was fit in the range 2.669-8.715 Å⁻¹. The residual of the fit was 1.2 %.

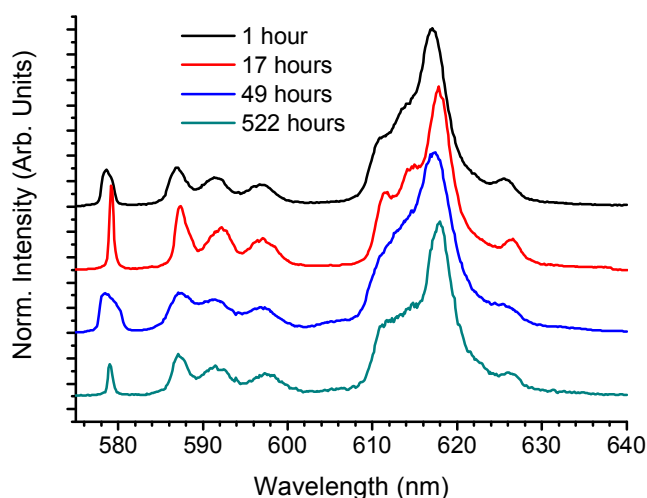
Figure 4 TRIFS of Cm³⁺ in synthetic apatite and bio-apatite a) Emission spectra with broad peak due to poorly defined Cm³⁺ environment centered at 607 nm. b) Fluorescence lifetime measurement indicating incorporation and multiple environments. c) Excitation spectrum of biologically produced hydroxyapatite indicating range of species as would be expected from an amorphous environment with large shoulder due to hot band excitation.

Figure 5 Fluorescence line narrowing in TRIFS of Cm³⁺ containing bio-apatite from direct excitation proving the presence of a continuum of related environments as would be expected by the incorporation into amorphous grain boundaries.

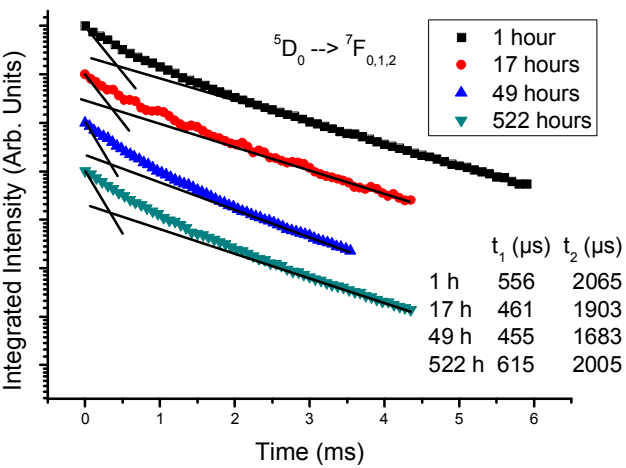
Supplementary Figure 1 TRIFS emission spectrum of sintered Eu³⁺ doped hydroxyapatite. This can be compared to established spectra of Eu³⁺ substituted in the Ca(II) site of apatite¹⁵⁻¹⁷. This spectrum in no way resembles the speciation seen before heating proving that the Ca(II) site can be ruled out as the incorporated species before heating.

Figures

Figure 1a

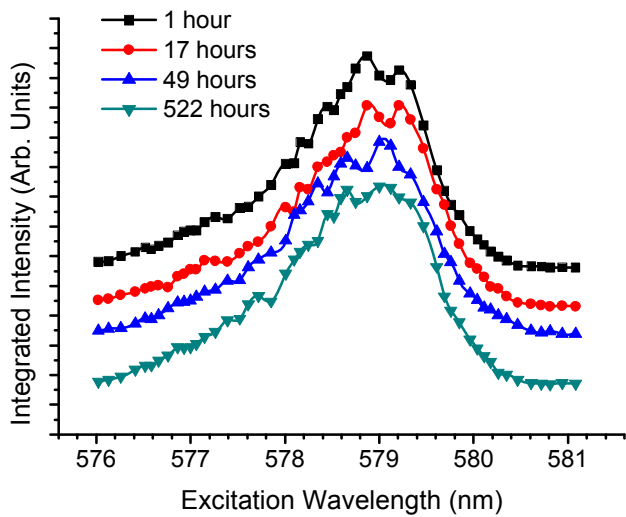


365 Figure 1b



366

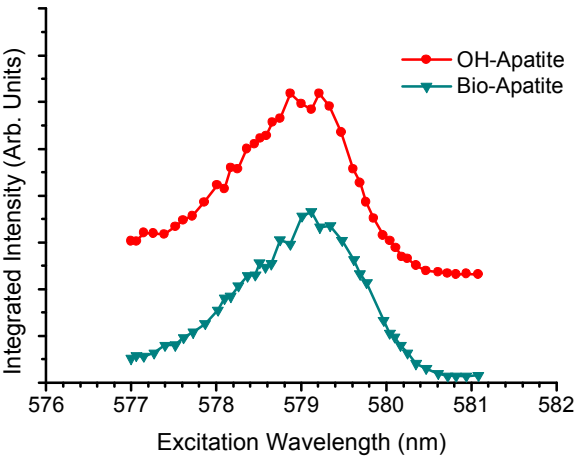
367 Figure 1c



368

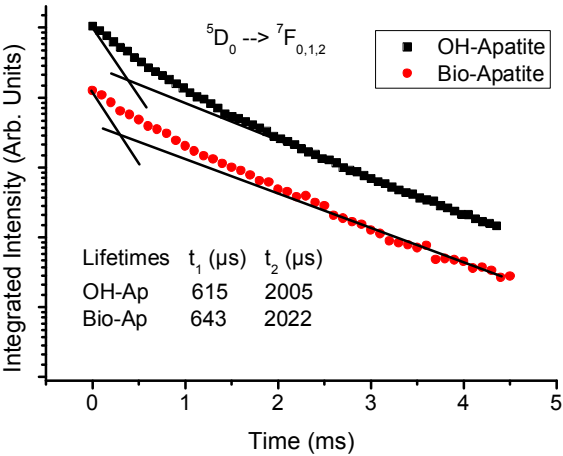
369

370 Figure 2a



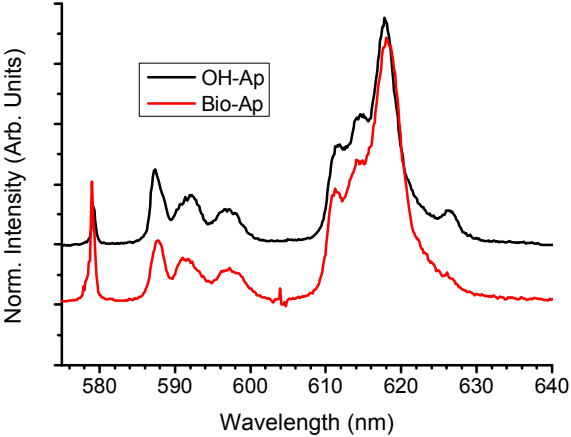
371

372 Figure 2b



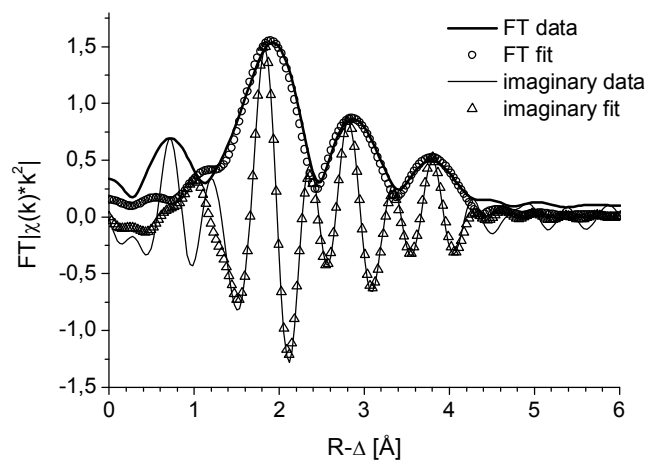
373

374 Figure 2c



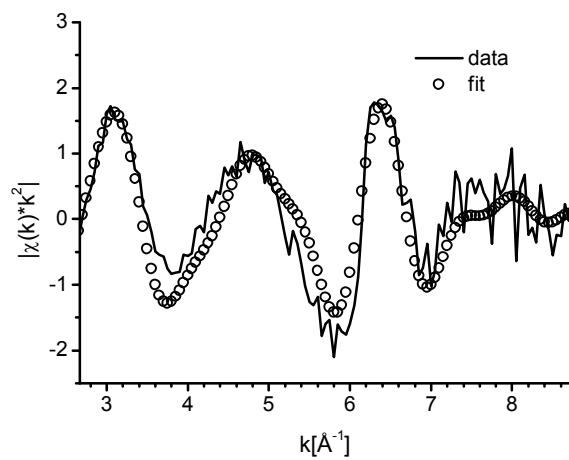
375

376 Figure 3a



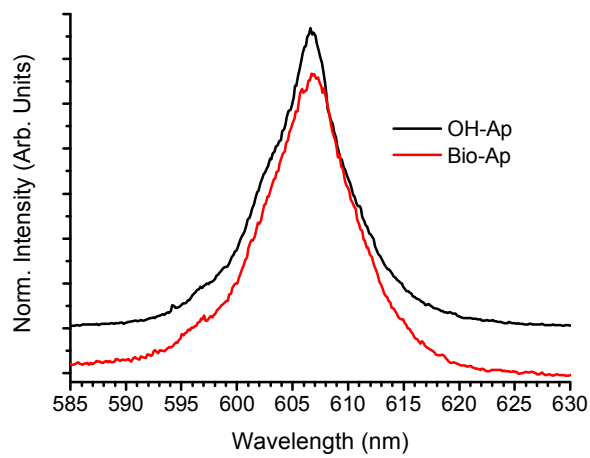
377

378 Figure 3b



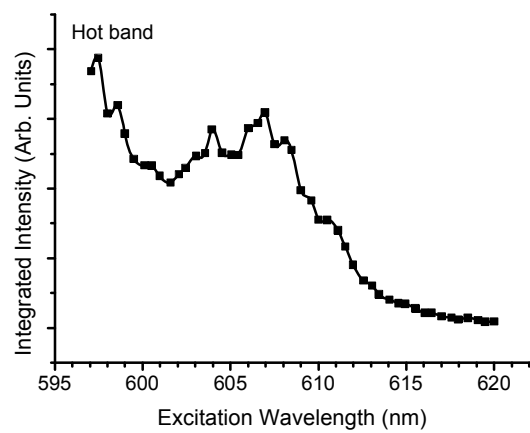
379

380 Figure 4a



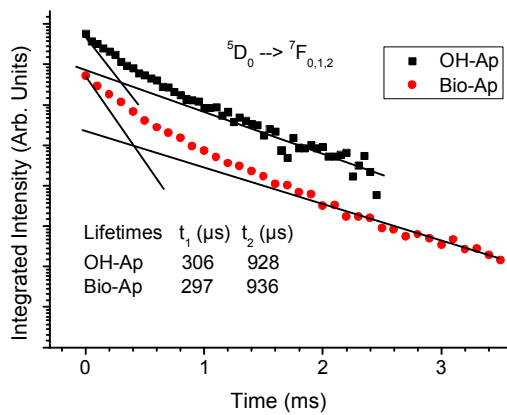
381

382 Figure 4b



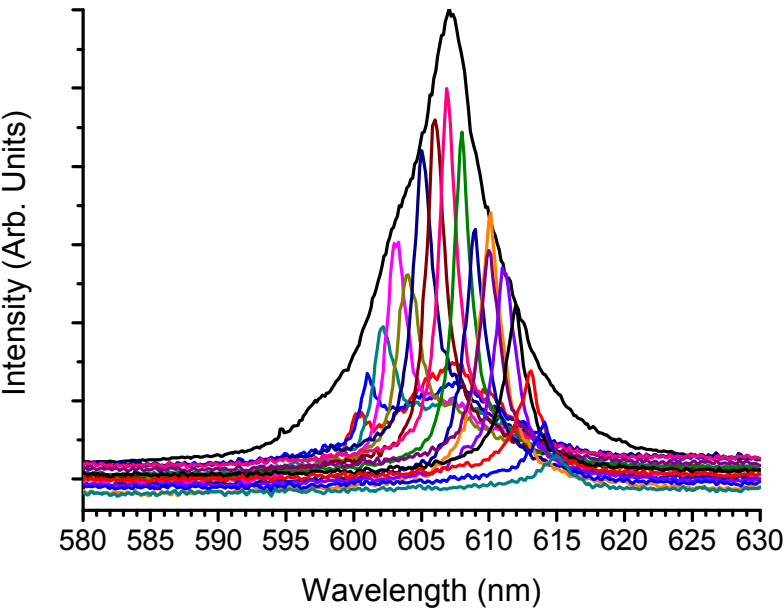
383

384 Figure 4c



385

386

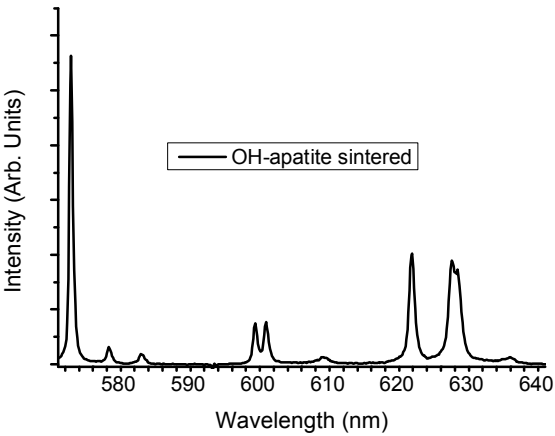


388

389 **Supplemental Material**

390 **Supplemental Table 1 EXAFS fitted parameter of synthetic apatite (OH-Ap) and biologically**
391 **produced apatite (Bio-Ap).** Typical error associated with coordination number is 20 % while
392 reported bond distances are ± 0.02 Å. Residual of fit was 0.88 %.

System	Bond	R (Å)	N	σ^2 (Å ²)	E _o (eV)
OH-Ap	Eu - O	2.39	7.9	0.004	4.6
Bio-Ap	Eu - O	2.41	7.0	0.005	0.9
OH-Ap	Eu - P	3.21	4.2	0.0002	10.7
Bio-Ap	Eu - P	3.26	1.3	0.005	16.0
OH-Ap	Eu - Ca	4.11	3.7	0.0004	11.8
Bio-Ap	Eu - Ca	-	-	-	-



394

395

